nature

https://doi.org/10.1038/s41586-024-07764-8

Accelerated Article Preview

Two-dimensional Perovskitoids Enhance Stability in Perovskite Solar Cells

Received: 6 February 2024

Accepted: 27 June 2024

Accelerated Article Preview

Cite this article as: Liu, C. et al. Two-dimensional Perovskitoids Enhance Stability in Perovskite Solar Cells. *Nature* https://doi.org/10.1038/s41586-024-07764-8 (2024)

Cheng Liu, Yi Yang, Hao Chen, Ioannis Spanopoulos, Abdulaziz S. R. Bati, Isaiah W. Gilley, Jianhua Chen, Aidan Maxwell, Badri Vishal, Robert P. Reynolds, Taylor E. Wiggins, Zaiwei Wang, Chuying Huang, Jared Fletcher, Yuan Liu, Lin X. Chen, Stefaan De Wolf, Bin Chen, Ding Zheng, Tobin J. Marks, Antonio Facchetti, Edward H. Sargent & Mercouri G. Kanatzidis

This is a PDF file of a peer-reviewed paper that has been accepted for publication. Although unedited, the content has been subjected to preliminary formatting. Nature is providing this early version of the typeset paper as a service to our authors and readers. The text and figures will undergo copyediting and a proof review before the paper is published in its final form. Please note that during the production process errors may be discovered which could affect the content, and all legal disclaimers apply.

ACCELERATED ARTICLE PREVIEW

Two-dimensional Perovskitoids Enhance Stability in Perovskite Solar Cells

Cheng Liu[1,7], Yi Yang[1,7], Hao Chen[1,7], Ioannis Spanopoulos[1,2,7], Abdulaziz S. R. Bati[1,7], Isaiah W. Gilley[1], Jianhua Chen[1], Aidan Maxwell[3], Badri Vishal[4], Robert P. Reynolds[1], Taylor E. Wiggins[1], Zaiwei Wang[3], Chuying Huang[1], Jared Fletcher[1], Yuan Liu[5], Lin X. Chen[1], Stefaan De Wolf[4], Bin Chen[1], Ding Zheng[1,*], Tobin J. Marks[1,*], Antonio Facchetti[1,6,*], Edward H. Sargent[1,3,5,*], Mercouri G. Kanatzidis[1*]

[1]Department of Chemistry, Northwestern University, 2145 Sheridan Rd, Evanston, Illinois 60208, United States

[2]Department of Chemistry, University of South Florida, Tampa, Florida, 33620, United States

[3]Department of Electrical and Computer Engineering, University of Toronto, 35 St George Street, Toronto, Ontario, M5S 1A4, Canada

[4]KAUST Solar Center, Physical Sciences and Engineering Division, King Abdullah University of Science and Technology (KAUST), Thuwal, Kingdom of Saudi Arabia

[5]Department of Electrical and Computer Engineering, Northwestern University, 2145 Sheridan Rd, Evanston, Illinois 60208, United States

[6]School of Materials Science and Engineering, Georgia Institute of Technology, 771 Ferst Dr NW, Atlanta, Georgia 30332, United States

[7]These authors contributed equally: C.L., Y.Y., H.C., I.S., A.S.R.B.

*Corresponding Authors: D.Z (ding.zheng@northwestern.edu); A.F. (afacchetti6@gatech.edu); T.J.M (t-marks@northwestern.edu); E.H.S (ted.sargent@northwestern.edu); M.G.K. (m-kanatzidis@northwestern.edu)

Abstract: Two-dimensional (2D)/three-dimensional (3D) perovskite heterostructures have played a key role in advancing the performance of perovskite solar cells (PSCs)[1,2]. However, the migration of cations between 2D and 3D layers results in the disruption of octahedral networks that leads to degradation in performance over time[3,4]. We hypothesized that perovskitoids, with robust organic-inorganic networks enabled by edge- and face-sharing, could impede ion migration. We explored a set of perovskitoids of varying dimensionality, and found that cation migration within perovskitoid/perovskite heterostructures was suppressed compared to the 2D/3D perovskite case. Increasing the dimensionality of perovskitoids improves charge transport when they are interfaced with 3D perovskite surfaces – this the result of enhanced octahedral connectivity and out-of-plane orientation. The 2D perovskitoid $(A6BfP)_8Pb_7I_{22}$ (A6BfP: *N*-aminohexyl-benz[f]-phthalimide) provides efficient passivation of perovskite surfaces and enables uniform large-area perovskite films. Devices based on perovskitoid/perovskite heterostructures achieve a certified quasi-steady-state power conversion efficiency of 24.6% for centimeter-area PSCs. We removed the fragile hole transport layers and showed stable operation of the underlying perovskitoid/perovskite heterostructure at 85°C for 1,250 hours for encapsulated large-area devices in an air ambient.

ACCELERATED ARTICLE PREVIEW

Main Text: Organic-inorganic hybrid perovskite solar cells (PSCs) have experienced performance breakthroughs in recent years, with single-junction, small-sized (< 1 cm^2) devices now surpassing power conversion efficiencies (PCEs) of 26%[5-7]. Recent advances in efficiency are driven by improvements in interface passivation; one particular strategy has been the application of two-dimensional (2D) perovskite surface passivation layers[1,2]. However, active cations, especially under thermal stress, can disrupt the fragile corner-sharing octahedral connections within the perovskite structures and migrate between the 2D and three-dimensional (3D) perovskite layers[3,4]. This type of ion migration is known to accelerate film degradation, negatively impacting both the efficiency and stability of devices[8,9]. To date, no efficient PSCs (certified PCE > 20%) utilizing 2D perovskite passivation have survived 85°C under ISOS-L-3 testing protocols (Supplementary Table 1).

To address this issue, non-2D-perovskite ligand strategies have been developed; these limit spacer penetration into the perovskite lattice, suppressing surface ion migration, even under high temperatures[10,11]. These strategies, however, tend to result in trade-offs with spacer-perovskite surface interaction strength due to steric effects[11,12], limiting the efficacy of passivation, particularly on large-area perovskite films[10,11].

This motivated us to consider new routes to suppress cation diffusion while maximizing passivation. The goal of creating more robust octahedral networks prompted us to add edge-/face-sharing into the motif, something implemented in perovskitoids[13,14]. This in turn enabled us to consider molecules containing a longer ammonium group: bulky group separation distance, creating the opportunity for the passivating ammonium to pair with perovskite defect sites in need of termination.

Perovskitoids comprising heterocyclic[14,15], aromatic[16], and multi-alkyl[17-20] ammonium ligands have been explored, including as passivating materials. Until now, the resultant device performance has lain behind that of the best PSCs, likely due to the low conductivity, limited functionality, and phase impurities within surface perovskitoid layers. We took the view that a wide study of the design guidelines for perovskitoid composition, materials processing, morphology, and electronic properties, is needed on the path to high-performance perovskitoid/perovskite heterostructures.

Design and Synthesis of Perovskitoids

We began by screening spacer molecules for perovskitoid fabrication based on three key principles: 1) incorporating bulky organic ammonium cations, known as spacer cations, to separate inorganic layers[21,22]; 2) introducing inter-spacer forces, such as π-π interactions and hydrogen bonding, to exert enough chemical pressure on the metal-halide skeleton to induce mixed-connectivity structures[13,23]; 3) isolating the bulky moieties, such as conjugated groups, from the ammonium-heads via carbon chains to enable coordination between the ammonium heads and metal halides[11,12].

We therefore explored spacers featuring distinct shapes and sizes of aromatic pthalimide moieties (Fig. 1a), namely *N*-aminohexyl-phthalimide hydroiodide (A6PI), *N*-aminohexyl-benz[f]-phthalimide hydroiodide (A6BfPI), *N*-aminohexyl-benz[e]-phthalimide hydroiodide (A6BePI), and *N*-aminohexyl-naphthalimide hydroiodide (A6NI).

ACCELERATED ARTICLE PREVIEW

To template the growth of perovskitoid structures, we synthesized single-crystals of the corresponding hybrid organic-inorganic iodoplumbates and iodostannates for each spacer by reacting the organic-halide salts of A6PI, A6BfPI, A6BePI, and A6NI with PbO or $SnCl_2 \cdot 2H_2O$ in an acid mixture of HI and H_3PO_2. The structures of the resulting single-crystals were elucidated through single-crystal X-ray diffraction (SCXRD), revealing crystallization in $P2_1/c$, $C2/c$, and P-1 space groups (details and Cambridge Crystallographic Data Centre (CCDC) numbers of single crystals are provided in Supplementary Fig. 1-8 and Supplementary Table 2-8).

(A6P)PbI_3, (A6P)SnI_3, (A6BfP)PbI_3, (A6BeP)PbI_3, and (A6N)SnI_3 are isostructural and crystallize in the monoclinic space group $P2_1/c$, forming 1D perovskitoid structures consisting of face-sharing $^1_\infty[MI_3]^-$ (M = Pb or Sn) octahedral chains (Fig. 1b and Supplementary Fig. S1-7). Despite the engagement of H_2O, (A6N)$_2$(H_5O_2)Pb_3I_9 also forms a 1D structure and crystallizes in the monoclinic space group $C2/c$ (Fig. 1b and Supplementary Fig. 6).

(A6BfP)$_8Sn_7I_{22}$ is the only one of these perovskitoids to crystallize in the triclinic space group P-1 and form a 2D structure comprised of $^2_\infty[Sn_7I_{22}]^{8-}$ sheets with a combination of corner-, edge-, and face-shared octahedral connections (Fig. 1c and Supplementary Fig. 4). We encountered challenges in synthesizing bulk (A6BfP)$_8Pb_7I_{22}$ single crystals despite the various single-crystal synthesis methods attempted, including slow cooling evaporation from acid and acetonitrile, as well as hydro- and solvothermal syntheses. It is noteworthy that the XRD pattern of the solution processed (A6BfP)$_8Pb_7I_{22}$ film exhibits primary diffraction peaks at 3.6 and 7.2°, precisely matching the (1 0 0) and (2 0 0) peaks of the simulated XRD pattern of (A6BfP)$_8Pb_7I_{22}$. This simulated pattern was approximated by manually replacing the tin atoms in the crystallographic information file (CIF) of (A6BfP)$_8Sn_7I_{22}$ with lead (Supplementary Fig. 8).

Perovskitoid/perovskite heterostructures

We then attempted to construct perovskitoid/perovskite heterostructures by dynamically casting an isopropanol solution containing these organic halide salts onto 3D Pb-based perovskite films[24]. We investigated the resulting films by using X-ray diffraction (Fig. 2a and Supplementary Fig. 9) and found that the films treated with A6PI and A6BfPI showed new, additional diffraction peaks, indicating the formation of a crystalline phase atop the 3D perovskite. However, the films treated with A6BePI and A6NI solutions showed no Bragg diffraction peaks, instead exhibiting broad, diffuse scattering, indicating the formation of amorphous phases. The primary new diffraction peak of the film treated with A6P, located at 6.2° 2θ, was aligned with the (0 0 2) peak of the simulated (A6P)PbI_3 diffraction pattern, which suggests that the crystalline phase obtained matches the 1D phase produced in the single-crystal synthesis. However, the new peaks observed at 3.6 and 7.2° 2θ on the film treated with A6BfPI diverge from the simulated diffraction pattern of the 1D (A6BfP)PbI_3 perovskitoid identified by SCXRD. Instead, these new peaks closely match with the (1 0 0) and (2 0 0) peaks of the simulated pattern of the (A6BfP)$_8Pb_7I_{22}$ perovskitoid, suggesting that the 2D perovskitoid was kinetically stabilized after deposition atop the 3D perovskite film. The (A6BfP)$_8Pb_7I_{22}$ perovskitoid/perovskite heterostructure was confirmed by cross-section TEM images (Supplementary Fig. 10).

Angle-dependent grazing-incidence wide-angle X-ray scattering (GIWAXS) (Fig. 2b) was performed on the films treated with A6PI and A6BfPI. The distinct diffraction arcs were observed for (A6P)PbI_3 ($q \approx 4.4$ Å^{-1}) and (A6BfP)$_8Pb_7I_{22}$ ($q \approx 2.6$ and 5.2 Å^{-1}), primarily appearing at an incident angle of 0.1° and absent at 1.0°, confirming the location of perovskitoids only on the surface of 3D perovskite. It is noteworthy that the atop (A6P)PbI_3 exhibits diffraction arcs along

ACCELERATED ARTICLE PREVIEW

the q_z axis, indicating an in-plane orientation of the (0 0 2) crystal plane. In contrast, the surface of $(A6BfP)_8Pb_7I_{22}$ shows diffraction arcs along both q_{xy} and q_z axes, indicating both out-of- and in-plane orientations of (1 0 0) and (2 0 0) crystal planes. The mixed orientations could provide fluent charge transport pathways through 2D perovskitoid layers (Fig. 2c)[25,26]. Surface-sectional scanning electron microscopy (SEM) images (Supplementary Fig. 11) indicated that the deposition of perovskitoids does not induce obvious alterations in grain sizes or surface morphologies of 3D perovskite films.

Perovskitoid passivation and stability

X-ray photoelectron spectroscopy (XPS) spectra (Fig. 3a) show that the Pb 4*f* peaks of perovskite films passivated with both 1D $(A6P)PbI_3$ and 2D $(A6BfP)_8Pb_7I_{22}$ perovskitoids shifted toward lower binding energy of over 0.8 eV compared with the control film, indicating increased local electron density. Films passivated by the widely used 2D perovskite $(PEA)_2PbI_4$ (PEA: phenylethylammonium) and non-2D ligand ortho-(phenylene)di(ethylammonium) iodide (*o*-$PDEAI_2$) were also examined for comparison[10,27]. They both led to smaller peak shifts (<0.5 eV) than the perovskitoids, which can be attributed to the fewer functional groups, and the sterically-weakened interactions between the non-2D ligand and $[PbI_6]^{4-}$ octahedra[11,12]. Time-resolved photoluminescence (TRPL) analysis reveals that non-2D ligand passivation increases the carrier lifetime from 0.48 μs to 0.60 μs, while the perovskitoid passivation doubles it to 0.98 μs (Supplementary Fig. 12 and Table 9).

We then sought to assess film uniformity by analyzing the photoluminescence (PL) intensity distribution on centimeter-scale perovskite films. The narrower PL intensity distribution observed in perovskitoid-passivated perovskite films indicates greater spatial homogeneity over large areas compared to 2D perovskite- and non-2D ligand-passivated perovskite films (Fig. 3b and Supplementary Fig. 13).

To assess the impact of the perovskitoid passivation strategy on photovoltaic performance, we fabricated PSCs with the structure of FTO/SnO_2/perovskite/passivation layer/2,2',7,7'-Tetrakis[*N,N*-di(4-methoxyphenyl)amino]-9,9'-spirobifluorene (*spiro*-OMeTAD)/Au, excluding the influence of isopropanol solvent (Supplementary Fig. 14). As depicted in Fig. 3c and Supplementary Fig. 15, the passivation with 2D perovskitoid $(A6BfP)_8Pb_7I_{22}$ results in higher device performance compared to the 1D perovskitoid $(A6P)PbI_3$. The superior performance of the $(A6BfP)_8Pb_7I_{22}$ compared to $(A6P)PbI_3$ we attribute to its higher dimensionality and increased degree of corner-sharing octahedral connection (Fig. 1b, c)[28-30]. $(A6BfP)_8Pb_7I_{22}$ introduces additional out-of-plane orientations atop perovskite films, in contrast with $(A6P)PbI_3$, consistent with its improved charge transport properties (Fig. 2b, c and Supplementary Fig. 16)[31].

We sought next to evaluate the stability of $(PEA)_2PbI_4$ and $(A6BfP)_8Pb_7I_{22}$ films under elevated temperature conditions of 85°C at 85% relative humidity (RH) using time-dependent XRD (Fig. 3d). For the traditional $(PEA)_2PbI_4$ sample, the diffraction peak at 5.4°, indexed to the (0 0 2) crystal plane, gradually decreased over time, accompanied by the emergence of a new peak at 12.7° corresponding to (0 0 1) PbI_2. This observation suggests that $(PEA)_2PbI_4$ exhibits a degree of thermal instability, in accord with prior reports[32]. In contrast, the XRD patterns for $(A6BfP)_8Pb_7I_{22}$ exhibited no apparent changes.

We then used time-dependent XRD to examine the stability of 2D/3D heterostructures, i.e. 2D $(PEA)_2PbI_4$/3D perovskite and 2D $(A6BfP)_8Pb_7I_{22}$/3D perovskite, following annealing at 85°C

ACCELERATED ARTICLE PREVIEW

under 85% RH (Fig. 3e). The intensity of the diffraction peak at 5.4˚ related to $(PEA)_2PbI_4$ decreased over time, disappearing entirely after 3 hours. This observation suggests the instability of the formed 2D perovskite layer, attributed to ion migration from the 2D structure into the bulk 3D perovskite, which was confirmed by the spacer distribution measured by time-of-flight secondary ion mass spectrometry (TOF-SIMS) as shown in Fig. 3f. In contrast, the diffraction peaks at 3.6˚ and 7.2˚ as well as spacer distribution associated with the $(A6BfP)_8Pb_7I_{22}$ remained relatively unchanged, indicating the superior stability of the perovskitoid/perovskite heterostructure under accelerated aging conditions.

In addition to the improved octahedral connection and the bulkier spacers, the inhibited cation diffusion within the heterostructure was also ascribed to the additional π-π attractive interactions between parallelly aligned A6BfP spacers within $(A6BfP)_8Pb_7I_{22}$, contributing to the structural cohesion, as evidenced by the intermolecular distance of ~3.2 Å (Supplementary Fig. 17). This is in contrast to the nonparallel orientation with wider intermolecular spacing within $(PEA)_2PbI_4$.

Device performance and stability

The current-voltage (*J-V*) scans of the champion small-area device (0.06 cm^2) based on $(A6BfP)_8Pb_7I_{22}$ passivation, seen in the cross-sectional SEM image in Fig. 4a, exhibit a PCE of 26.1% with a V_{OC} of 1.17 V, J_{SC} of 26.1 mA cm^{-2}, and FF of 85.4% (Fig. 4b), along with a stabilized PCE of 25.6% (Supplementary Fig. 18). The bandgap of the devices was determined from the external quantum efficiency (EQE) spectrum (Fig. 4c) to be ~1.53 eV.

We assessed the applicability of our perovskitoid passivation approach to larger-area devices, obtaining an in-lab PCE of 25.1% for devices having an active area of 1 cm^2 (Fig. 4d). We further sent a device to the accredited Newport Photovoltaic Testing and Calibration Laboratory in the US for certification, and these were certified to have a quasi-steady-state (QSS) PCE of 24.6% for an illuminated area of 1.04 cm^2 following the asymptotic maximum power scan (AMPS) protocol (Fig. 4e and Supplementary Fig. 19). Certified stabilized PCEs for devices with 1 cm^2 areas are summarized and listed in Supplementary Table 10[33-35].

Motivated by these results, we fabricated perovskite modules having an aperture area of 27.6 cm^2: these had a stabilized PCE of 22.1% (Fig. 4f), placing them among the most efficient perovskite solar modules[36-39].

To elucidate the effect of 2D perovskite/perovskitoid passivation on device stability, we assessed the damp-heat stability of unencapsulated small cells at 85% RH and 85°C (ISOS-D-3 protocol, where ISOS is the International Summit on Organic PV stability). The $(A6BfP)_8Pb_7I_{22}$-based device retained 80% of its initial PCE after 240 hours due to the suppressed ion migration and enhanced water resistance of the surface perovskitoid layer (Fig. 4g and Supplementary Fig. 20). In comparison, the $(PEA)_2PbI_4$-based device only retained 18% of its initial PCE under the same testing conditions.

We then investigated the long-term operating stability of encapsulated devices subjected to continuous 1-sun illumination at maximum power point (MPP) in ambient conditions (Fig. 4h). The fragile spiro-OMeTAD was substituted with poly[bis(4-phenyl)(2,4,6-trimethylphenyl)amine] to eliminate the hole transport layer as a source of instability[7,40]. After continuous operation under 1 sun illumination at 85˚C (ISOS-L-3 protocol) for 1,250 hours, the $(A6BfP)_8Pb_7I_{22}$-based device retained 85% of its initial PCE, surpassing the $(PEA)_2PbI_4$-based

ACCELERATED ARTICLE PREVIEW

device which exhibited 52% PCE retention. A comparison with other 1 cm^2 PSCs with regards to operating stability is presented in Supplementary Table 11.

The integration of perovskitoid passivation brings the benefit of impeding cation migration and militating against carrier recombination at the interface, resulting in enhanced operating stability at elevated temperatures, this combined with increased PCE at large areas.

Reference

1 Grancini, G. *et al.* One-Year stable perovskite solar cells by 2D/3D interface engineering. *Nat. Commun.* **8**, 15684 (2017). https://doi.org/10.1038/ncomms15684

2 Sidhik, S. *et al.* Deterministic fabrication of 3D/2D perovskite bilayer stacks for durable and efficient solar cells. *Science* **377**, 1425-1430 (2022). https://doi.org/doi:10.1126/science.abq7652

3 Luo, L. *et al.* Stabilization of 3D/2D perovskite heterostructures via inhibition of ion diffusion by cross-linked polymers for solar cells with improved performance. *Nat. Energy* **8**, 294-303 (2023). https://doi.org/10.1038/s41560-023-01205-y

4 Szabó, G. & Kamat, P. V. How Cation Migration across a 2D/3D interface dictates perovskite solar cell efficiency. *ACS Energy Lett.*, 193-200 (2023). https://doi.org/10.1021/acsenergylett.3c02503

5 Liu, C. *et al.* Bimolecularly passivated interface enables efficient and stable inverted perovskite solar cells. *Science* **382**, 810-815 (2023). https://doi.org/doi:10.1126/science.adk1633

6 Chen, H. *et al.* Improved charge extraction in inverted perovskite solar cells with dual-site-binding ligands. *Science* 384, 189-193 (2024). https://doi.org/doi:10.1126/science.adm9474

7 Zhao, Y. *et al.* Inactive $(PbI_2)_2RbCl$ stabilizes perovskite films for efficient solar cells. *Science* **377**, 531-534 (2022). https://doi.org/doi:10.1126/science.abp8873

8 Perini, C. A. R. *et al.* Interface reconstruction from Ruddlesden–Popper structures impacts stability in lead halide perovskite solar cells. *Adv. Mater.* **34**, 2204726 (2022). https://doi.org/10.1002/adma.202204726

9 Chakkamalayath, J., Hiott, N. & Kamat, P. V. How stable is the 2D/3D interface of metal halide perovskite under light and heat? *ACS Energy Lett.* **8**, 169-171 (2023). https://doi.org/10.1021/acsenergylett.2c02408

10 Liu, C. *et al.* Tuning structural isomers of phenylenediammonium to afford efficient and stable perovskite solar cells and modules. *Nat. Commun.* **12**, 6394 (2021). https://doi.org/10.1038/s41467-021-26754-2

11 Park, S. M. *et al.* Engineering ligand reactivity enables high-temperature operation of stable perovskite solar cells. *Science* **381**, 209-215 (2023). https://doi.org/10.1126/science.adi4107

12 Jiang, Y. *et al.* Synthesis-on-substrate of quantum dot solids. *Nature* **612**, 679-684 (2022). https://doi.org/10.1038/s41586-022-05486-3

13 Li, X. *et al.* Three-dimensional lead iodide perovskitoid hybrids with high X-ray photoresponse. *J. Am. Chem. Soc.* **142**, 6625-6637 (2020). https://doi.org/10.1021/jacs.0c00101

14 Gao, L. *et al.* Improved environmental stability and solar cell efficiency of $(MA,FA)PbI_3$ perovskite using a wide-band-gap 1D thiazolium lead iodide capping layer strategy. *ACS Energy Lett.* **4**, 1763-1769 (2019). https://doi.org/10.1021/acsenergylett.9b00930

15 Semerci, A. *et al.* A novel multi-functional thiophene-based organic cation as passivation, crystalline orientation, and organic spacer agent for low-dimensional 3D/1D perovskite solar cells. *Adv. Opt. Mater.* 11, 2300267 (2023). https://doi.org/10.1002/adom.202300267

16 Chen, J. *et al.* Highly efficient and stable perovskite solar cells enabled by low-dimensional perovskitoids. *Sci. Adv*. 8, eabk2722 (2022). https://doi.org/doi:10.1126/sciadv.abk2722

17 Kong, T. *et al.* Perovskitoid-templated formation of a 1D@3D perovskite structure toward highly efficient and stable perovskite solar cells. *Adv. Energy Mater.* 11, 2101018 (2021). https://doi.org/10.1002/aenm.202101018

ACCELERATED ARTICLE PREVIEW

18 Wang, H. *et al.* Water stable haloplumbate modulation for efficient and stable hybrid perovskite photovoltaics. *Adv. Energy Mater.* 11, 2101082 (2021). https://doi.org/10.1002/aenm.202101082
19 Miao, Y. *et al.* Green solvent enabled scalable processing of perovskite solar cells with high efficiency. *Nat. Sustain.* 6, 1465-1473 (2023). https://doi.org/10.1038/s41893-023-01196-4
20 Zhang, F. *et al.* Surface lattice engineering through three-dimensional lead iodide perovskitoid for high-performance perovskite solar cells. *Chem* 7, 774-785 (2021). https://doi.org/10.1016/j.chempr.2020.12.023
21 Li, X., Hoffman, J. M. & Kanatzidis, M. G. The 2D halide perovskite rulebook: how the spacer influences everything from the structure to optoelectronic device efficiency. *Chem. Rev.* **121**, 2230-2291 (2021). https://doi.org/10.1021/acs.chemrev.0c01006
22 Mao, L., Stoumpos, C. C. & Kanatzidis, M. G. Two-dimensional hybrid halide perovskites: principles and promises. *J. Am. Chem. Soc.* **141**, 1171-1190 (2019). https://doi.org/10.1021/jacs.8b10851
23 Kamminga, M. E. *et al.* Confinement effects in low-dimensional lead iodide perovskite hybrids. *Chem. Mater.* **28**, 4554-4562 (2016). https://doi.org/10.1021/acs.chemmater.6b00809
24 Ansari, F. *et al.* Passivation mechanism exploiting surface dipoles affords high-performance perovskite solar cells. *J. Am. Chem. Soc.* **142**, 11428-11433 (2020). https://doi.org/10.1021/jacs.0c01704
25 Kim, H. *et al.* Self-crystallized multifunctional 2D perovskite for efficient and stable perovskite solar cells. *Adv. Funct. Mater.* **30**, 1910620 (2020). https://doi.org/10.1002/adfm.201910620
26 Yang, Y. *et al.* Universal approach toward high-efficiency two-dimensional perovskite solar cells via a vertical-rotation process. *Energy Environ. Sci.* **13**, 3093-3101 (2020). https://doi.org/10.1039/D0EE01833C
27 Cho, K. T. *et al.* Selective growth of layered perovskites for stable and efficient photovoltaics. *Energy Environ. Sci.* **11**, 952-959 (2018). https://doi.org/10.1039/C7EE03513F
28 Gao, P., Bin Mohd Yusoff, A. R. & Nazeeruddin, M. K. Dimensionality engineering of hybrid halide perovskite light absorbers. *Nat. Commun.* **9**, 5028 (2018). https://doi.org/10.1038/s41467-018-07382-9
29 Hoye, R. L. Z. *et al.* The role of dimensionality on the optoelectronic properties of oxide and halide perovskites, and their halide derivatives. *Adv. Energy Mater.* **12**, 2100499 (2022). https://doi.org/10.1002/aenm.202100499
30 Hartono, N. T. P. *et al.* The effect of structural dimensionality on carrier mobility in lead-halide perovskites. *J. Mater. Chem. A* **7**, 23949-23957 (2019). https://doi.org/10.1039/C9TA05241K
31 Niu, T. *et al.* Interfacial engineering at the 2D/3D heterojunction for high-performance perovskite solar cells. *Nano Lett.* **19**, 7181-7190 (2019). https://doi.org/10.1021/acs.nanolett.9b02781
32 Zhao, R. *et al.* Rigid conjugated diamine templates for stable Dion–Jacobson-type two-dimensional perovskites. *J. Am. Chem. Soc.* **143**, 19901-19908 (2021). https://doi.org/10.1021/jacs.1c09515
33 Peng, J. *et al.* Centimetre-scale perovskite solar cells with fill factors of more than 86 per cent. *Nature* **601**, 573-578 (2022). https://doi.org/10.1038/s41586-021-04216-5
34 Li, J. *et al.* Enhancing the efficiency and longevity of inverted perovskite solar cells with antimony-doped tin oxides. *Nat. Energy* (2024). https://doi.org/10.1038/s41560-023-01442-1
35 Zhou, J. *et al.* Highly efficient and stable perovskite solar cells via a multifunctional hole transporting material. *Joule* (2024). https://doi.org/10.1016/j.joule.2024.02.019
36 Shi, P. *et al.* Oriented nucleation in formamidinium perovskite for photovoltaics. *Nature* **620**, 323-327 (2023). https://doi.org/10.1038/s41586-023-06208-z
37 Ding, Y. *et al.* Single-crystalline TiO_2 nanoparticles for stable and efficient perovskite modules. *Nat. Nanotechnol.* **17**, 598-605 (2022). https://doi.org/10.1038/s41565-022-01108-1
38 Liu, C. *et al.* Retarding solid-state reactions enable efficient and stable all-inorganic perovskite solar cells and modules. *Sci. Adv.* **9**, eadg0087 (2023) https://doi.org/10.1126/sciadv.adg0087
39 Yang, Y. *et al.* A thermotropic liquid crystal enables efficient and stable perovskite solar modules. *Nat. Energy* **9**, 316-323 (2024). https://doi.org/10.1038/s41560-023-01444-z

ACCELERATED ARTICLE PREVIEW

40 Zhao, Y. *et al.* A bilayer conducting polymer structure for planar perovskite solar cells with over 1,400 hours operational stability at elevated temperatures. *Nat. Energy* **7**, 144-152 (2022). https://doi.org/10.1038/s41560-021-00953-z

ACCELERATED ARTICLE PREVIEW

Fig. 1 | Design and synthesis of perovskitoids. a. Molecular structures of *N*-aminohexyl-phthalimide hydroiodide (A6PI), *N*-aminohexyl-benz[f]-phthalimide hydroiodide (A6BfPI), *N*-aminohexyl-benz[e]-phthalimide hydroiodide (A6BePI), and *N*-aminohexyl-naphthalimide hydroiodide (A6NI). **b.** Side-view of single crystals of $(A6P)PbI_3$, $(A6BfP)PbI_3$, $(A6BeP)PbI_3$, and $(A6N)PbI_3$. **c.** Crystal structure of $(A6BfP)_8Sn_7I_{22}$. Carbon, nitrogen, oxygen, lead, tin, and iodine are shown in black, blue, red, gray, lavender, and purple, respectively. Hydrogens are omitted for visual clarity.

Fig. 2 | Construction of perovskitoid/perovskite heterostructures. a. Experimental XRD patterns (top) of 3D/$(A6P)PbI_3$, 3D/$(A6BfP)_8Pb_7I_{22}$, 3D/A6BePI and 3D/A6NI; and simulated XRD spectra (bottom) of $(A6P)PbI_3$, $(A6BfP)_8Pb_7I_{22}$, $(A6BeP)PbI_3$ and $(A6N)PbI_3$. **b.** GIWAXS patterns of the 1D $(A6N)PbI_3$/ and 2D $(A6BfP)_8Pb_7I_{22}$/3D perovskite heterostructure films at incident angles of 0.1° (left) and 1.0° (right). **c.** Schematic representation of orientations of the atop 1D $(A6N)PbI_3$ and 2D $(A6BfP)_8Pb_7I_{22}$ on 3D perovskite films.

Fig. 3 | Characteristics of 2D/3D heterostructures. a. High-resolution Pb 4*f* XPS peaks and **b.** PL intensity statistics of 3D perovskite films passivated by non-2D ligand, 2D perovskite $(PEA)_2PbI_4$ and 2D perovskitoid $(A6BfP)_8Pb_7I_{22}$. In each condition, 16 data points were collected over a 2 × 2 cm region. Solid lines represent the statistical distribution curve fitted using a Gaussian distribution model. σ is the standard deviation. **c.** Efficiency statistics of PSCs as a function of passivation strategy. Twelve devices were evaluated at each condition, utilizing a reverse scan approach with a scanning step of 20 mV and a scanning rate of 70 mV/s. In the boxplots, the mean (open square), median (centre line), 25^{th} and 75^{th} percentiles (box bounds) are shown. **d.** Time-dependent XRD patterns of $(PEA)_2PbI_4$ and $(A6BfP)_8Pb_7I_{22}$ films under 85% RH and 85°C. **e.** Time-dependent XRD of 3D perovskite films with passivation of 2D $(PEA)_2PbI_4$ and 2D $(A6BfP)_8Pb_7I_{22}$ under 85% RH and 85°C. **f**. Time-of-flight secondary ion mass spectrometry (TOF-SIMS) of 2D $(PEA)_2PbI_4$/3D perovskite and 2D $(A6BfP)_8Pb_7I_{22}$/3D perovskite before and after aging for 3 hours under 85% RH and 85°C.

Fig. 4 | Photovoltaic performance. a. Cross-sectional SEM image of the target PSC. **b.** *J-V* characteristics of the champion small-area device. **c**. EQE curves and integrated current density of the 2D perovskitoid/3D perovskite-based device. **d.** *J-V* curve of a champion large-area (>1 cm^2) device. **e.** The QSS *J-V* curve of a representative $(A6BfP)_8Pb_7I_{22}$-based 1 cm^2 device certified at Newport, following asymptotic maximum power scan (AMPS) protocols. **f.** *J-V* curve and SPO of perovskite module with an aperture area of 28 cm^2. **g.** Periodic PCE evolution for the unencapsulated small-sized PSCs at 85% RH and 85°C. Data are presented as the mean value +/- the standard deviation (σ). **h.** MPPT for the 1 cm^2 devices measured at 85°C under continuous light illumination at 100 mW cm^{-2} in ambient conditions.

ACCELERATED ARTICLE PREVIEW

Methods

Materials. All materials were used as received without further purification. $SnCl_2 \cdot 2H_2O$ (99.99%), urea (99%), HCl acid (37 wt. % in water), thioglycolic acid (TGA, 98%), CsI (99.99%), 4-tert-Butylpyridine (98%), and bis(trifluoromethanesulfonyl)-imide lithium salt (LiTFSI, 99.0%) were purchased from Sigma-Aldrich. PbI_2 (99.99%) were purchased from TCI America™. Formamidinium iodide (FAI), methylammonium chloride (MACl), methylammonium iodide (MAI), phenylethylammonium iodide (PEAI), and FK209 Co(III) TFSI salt were purchased from Greatcell Solar Materials. *N,N*-dimethylformamide (DMF, 99.8%), dimethyl sulfoxide (DMSO, 99.7%), isopropanol (99.8%), acetonitrile (99.9%), and chlorobenzene (99.8%) were purchased from MilliporeSigma. PbO (99.9%) were purchased from Alfa Aesar. Hydroiodic acid (57 wt%), hypophosphorous acid (50 wt%), and $SnCl_2 \cdot 2H_2O$ (98%) was purchased from Sigma-Aldrich. Spiro-OMeTAD and poly[bis(4-phenyl)(2,4,6-trimethylphenyl)amine] were from the Xi'an Yuri Solar Co. Ltd.

Synthesis of ammonium salts.

The synthetic route and NMR data of ammonium salts are shown in Supplementary Fig. S21-29. N-Boc-1,6-diaminohexane (2.16 g, 10.0 mmol) was added to a suspension of corresponding dicarboxylic anhydride (10.0 mmol) in 50 mL ethanol and the resulting mixture was refluxed for 3 hours. The excess ethanol was then evaporated under reduced pressure until a large amount of white precipitate appeared. The precipitate was filtered and dried under a vacuum. The precipitate was then dissolved in diethyl ether (50 mL) and treated with excess hydriodic acid (2 mL, 55-57 wt.% solution in H_2O). The product salt was then obtained by filtration, washed with Et_2O, and dried under vacuum.

A6PI was obtained as a bright yellow solid (2.85 g, yield: 76%). ^{1}H NMR (500 MHz, MeOD) δ (ppm): 7.88 – 7.84 (m, 2H), 7.83 – 7.79 (m, 2H), 3.70 (t, *J* = 7.1 Hz, 2H), 2.96 (t, *J* = 7.6 Hz, 2H), 1.75 – 1.65(m, 4H), 1.56 – 1.35 (m, 4H). ^{13}C NMR (126 MHz, MeOD) δ (ppm): 168.50, 134.03, 131.94, 122.69, 39.29, 37.17, 27.88, 27.02, 25.91, 25.47.

A6BfP was obtained as a white solid (3.66 g, yield: 86%). ^{1}H NMR (500 MHz, MeOD) δ (ppm): 8.29 (s, 2H), 8.11 (dd, *J* = 6.1, 3.3 Hz, 2H), 7.73 (dd, *J* = 6.2, 3.2 Hz, 2H), 3.73 (t, *J* = 7.1 Hz, 2H), 2.97 (t, *J* = 7.6 Hz, 2H), 1.82 – 1.66 (m, 4H), 1.55 – 1.39 (m, 4H). ^{13}C NMR (126 MHz, MeOD) δ (ppm): 168.13, 135.46, 129.98, 129.05, 127.53, 124.08, 39.29, 37.41, 27.83, 27.03, 25.97, 25.49.

A6BePI was obtained as a white solid (3.51 g, yield: 83%). ^{1}H NMR (500 MHz, 500 MHz, MeOD) δ(ppm): 8.85 (d, *J* = 8.3 Hz, 1H), 8.26 (d, *J* = 8.2 Hz, 1H), 8.04 (d, *J* = 8.0 Hz, 1H), 7.79 (t, *J* = 16.1 Hz, 1H), 7.75 – 7.58 (m, 2H), 3.72 (t, *J* = 7.0 Hz, 2H), 2.94 (t, *J* = 7.2 Hz, 2H), 1.81 – 1.60 (m, 4H), 1.55 – 1.38 (m, 4H). ^{13}C NMR (126 MHz MeOD) δ (ppm): 169.55, 169.03, 136.73, 134.95, 131.19, 129.24, 128.70, 128.49, 127.71, 126.93, 124.09, 117.82, 39.29, 37.08, 28.07, 27.07, 25.97, 25.5.

A6NI was obtained as a white solid (3.23 g, yield: 76%). ^{1}H NMR (500 MHz, MeOD) δ (ppm): 8.46 (dd, *J* = 7.3, 1.0 Hz, 2H), 8.29 (dd, *J* = 8.3, 0.8 Hz, 2H), 7.81 – 7.74 (m, 2H), 4.17 – 4.07 (m, 2H), 2.98 (t, *J* = 7.6 Hz, 2H), 1.73 (tt, *J* = 15.2, 7.6 Hz, 4H), 1.59 – 1.43 (m, 4H). ^{13}C NMR (126 MHz, MeOD) δ (ppm): 164.11, 134.15, 131.66, 130.69, 127.67, 126.75, 122.05, 39.60, 39.32, 27.34, 27.02, 26.10, 25.61.

ACCEPTED ARTICLE PREVIEW

Synthesis of single crystals

(A6P)PbI_3: PbO powder (670 mg, 3 mmol) was dissolved in 57% w/w aqueous HI solution (6 mL) in a 20 mL glass scintillation vial by heating to boiling under constant magnetic stirring for about 5 min, which formed a bright yellow solution. Then 50 mg (0.13 mmol) of A6PI were added to the hot solution. Heating was discontinued and the solution was left to cool to RT directly. Yellow crystals deposited after a few hours.

(A6BfP)PbI_3: PbO powder (223 mg, 1 mmol) was dissolved in 57% w/w aqueous HI solution (7 mL) in a 20 mL glass scintillation vial by heating to boiling under constant magnetic stirring for about 5 min, which formed a bright yellow solution. Then 20 mg (0.05 mmol) of A6BfPI were added to the hot solution. Heating was discontinued and the solution was left to cool to RT directly. Yellow crystals deposited after a few hours.

(A6BeP)PbI_3: PbO powder (223 mg, 1 mmol) was dissolved in 57% w/w aqueous HI solution (7 mL) in a 20 mL glass scintillation vial by heating to boiling under constant magnetic stirring for about 5 min, which formed a bright yellow solution. Then 20 mg (0.05 mmol) of A6BePI were added to the hot solution. Heating was discontinued and the solution was left to cool to RT directly. Yellow crystals deposited after a few hours.

$(A6N)_2(H_5O_2)Pb_3I_9$: PbO powder (223 mg, 1 mmol) was dissolved in 57% w/w aqueous HI solution (7 mL) in a 20 mL glass scintillation vial by heating to boiling under constant magnetic stirring for about 5 min, which formed a bright yellow solution. Then 20 mg (0.05 mmol) of A6NI were added to the hot solution. Heating was discontinued and the solution was left to cool to RT directly. Orange crystals deposited after a few hours.

(A6P)SnI_3: $SnCl_2 \cdot 2H_2O$ (675 mg, 3 mmol) was dissolved in 57% w/w aqueous HI solution (4 mL) and 50% aqueous H_3PO_2 (4 mL) in a 20 mL glass scintillation vial by heating to boiling under constant magnetic stirring for about 5 min. Then 60 mg (0.16 mmol) of A6PI were added to the hot solution. Heating was discontinued and the solution was left to cool to RT directly. Yellow crystals deposited after a few hours.

$(A6BfP)_8Sn_7I_{22}$: $SnCl_2 \cdot 2H_2O$ (225 mg, 1 mmol) was dissolved in 57% w/w aqueous HI solution (4 mL) and 50% aqueous H_3PO_2 (4 mL) in a 20 mL glass scintillation vial by heating to boiling under constant magnetic stirring for about 5 min. Then 20 mg (0.05 mmol) of A6BfPI were added to the hot solution. Heating was discontinued and the solution was left to cool to RT directly. Orange crystals deposited after a few hours.

(A6N)SnI_3: $SnCl_2 \cdot 2H_2O$ (225 mg, 1 mmol) was dissolved in 57% w/w aqueous HI solution (4 mL) and 50% aqueous H_3PO_2 (4 mL) in a 20 mL glass scintillation vial by heating to boiling under constant magnetic stirring for about 5 min. Then 20 mg (0.05 mmol) of A6NI were added to the hot solution. Heating was discontinued and the solution was left to cool to RT directly. Red crystals deposited after a few hours.

Perovskitoid film preparation.

Perovskitoid film preparation. For the $(A6BfP)_8Pb_7I_{22}$ film, a 0.5 M solution of $(A6BfP)_8Pb_7I_{22}$ was prepared by dissolving 424 mg of A6BfPI and 231 mg of PbI_2 in 1 mL of DMF. Similarly, for the $(A6BfP)_8Sn_7I_{22}$ film, a 0.5 M solution was prepared by dissolving 242 mg of A6BfPI and 186 mg of SnI_2 in 1 mL of DMF. The perovskitoid solutions were spin-coated onto glass substrates

ACCELERATED ARTICLE PREVIEW

using a one-step process at 4000 rpm for 30 seconds, followed by annealing at 100°C for 10 minutes.

Solar cell fabrication.

The compact SnO_2 electron transporting layer (ETL) was deposited on precleaned FTO substrates using the chemical bath deposition (CBD) method. The substrates were immersed in a CBD solution containing 2.5 g of urea, 2.5 mL of HCl, 50 µL of TGA, and 550 mg of $SnCl_2 \cdot 2H_2O$ in 200 mL of deionized water that subsequently was placed in an oven at 90 °C for 5.5 hours. After cooling to room temperature, the substrates were washed with isopropanol followed by thermal annealing at 190°C for 1 hour before undergoing a UV ozone treatment for 30 min. The substrates were then transferred to a nitrogen-filled glove box for perovskite deposition. A 1.60 M $Cs_{0.05}MA_{0.05}FA_{0.9}PbI_3$ perovskite solution was prepared with extra 5 mol% PbI_2 and 30 mol% MACl in a mixed DMF and DMSO solution with a volume ratio of 7:3. Excess PbI_2 facilitates reaction with organic salts and the formation of perovskitoid layers on top of 3D perovskite films. The perovskite solution was spin coated onto the SnO_2 in a two-step process; first at 1000 rpm for 10 s and then 5000 rpm for 30 s. At the 20th second of the second step, 125 uL of chlorobenzene was poured onto the substrate followed by annealing at 100°C for 50 min and 150°C for 10 min. A 10 mM spacer solution (PEAI, A6PI, A6BfPI, A6BePI, and A6NI) in isopropanol was then dynamically spin-coated onto the perovskite films at 4500 rpm for 30 s followed by a post annealing at 100°C for 5 min. The hole transporting layer solution containing 0.06 M spiro-OMeTAD and 0.2 M 4-tert-butylpyridine in chlorobenzene, 0.03 M LiTFSI in acetonitrile, and 0.0035 M FK209 Co(III) TFSI salt in acetonitrile, was next deposited at 3000 rpm for 20 s at room temperature. Finally, 70 nm gold electrodes were thermally evaporated under a vacuum of 10^{-7} Torr.

Module fabrication.

Perovskite solar modules were constructed with eight sub-cells connected in series on 6.5 cm × 7 cm substrates. FTO substrates underwent laser scribing using a 1030 nm picosecond CO_2 laser operating at 3 W and a frequency of 200 kHz (LPKF ProtoLaser R). P1 lines, 50 µm in width, were employed to separate the sub-cells. The deposition procedures for the ETL, passivation layer, and HTL were consistent with those used for the fabrication of solar cells. Perovskite films were deposited using vacuum-flash solution processing (VASP) in a nitrogen-filled glovebox. The 1.3 M $Cs_{0.05}MA_{0.05}FA_{0.9}PbI_3$ perovskite precursor was spin-coated at 1000 rpm for 10 s and 5000 rpm for 20 s. Subsequently, the substrates were promptly transferred to a vacuum chamber and rapidly evacuated to a pressure of 2-5 Pa at 100°C. After 1 minute, the chamber was vented, and the perovskite films were annealed at 100 °C for 50 min and 150 °C for 10 min. P2 lines, 100 µm in width, were patterned using a 1030 nm picosecond CO_2 laser at 0.4 W and a frequency of 200 kHz (LPKF ProtoLaser R). Following gold deposition, P3 lines of the same width were laser-scribed to finalize the module fabrication, using the same laser, power, and frequency. The geometric fill factor (GFF) was 92%.

Characterization.

Single crystal diffraction experiments were performed on a Riguaku XtaLAB Synergy diffractometer equipped with a micro-focus sealed X-ray tube PhotonJet (Mo) X-ray source and a Hybrid Pixel Array Detector (HyPix) detector. Temperatures of the crystals were controlled with an Oxford Cryosystems low-temperature device. Data reduction was performed with the

ACCELERATED ARTICLE PREVIEW

CrysAlisPro software using numerical absorption correction. The structures were solved with the ShelXT and ShelXS structure solution programs using intrinsic phasing and direct methods solution methods, respectively and by using Olex2 as the graphical interface. The models were refined with ShelXL using least squares minimization. Simulated diffraction patterns were calculated based on CIFs refined from single-crystal diffraction experiments. Simulation was performed using the software Mercury with a wavelength of 1.54056 Å, a step of 0.02˚ 2θ, and a full-width at half-maximum of 0.1˚ 2θ.

The *J-V* characteristics were measured at room temperature in N_2 glovebox using a Keithley 2400 source under simulated AM 1.5 G irradiation (100 mW cm^{-2}). The irradiation was achieved using a Xe arc lamp from a Sciencetech A1 Light Line Class AAA solar simulator, which was calibrated with a reference solar cell (Sciencetech SCI-REF-Q) prior to measurement. No preconditioning was applied to the device before measurement. The scanning step for solar cells was set at 20 mV, while for modules, it was 128 mV, with a scanning rate of 70 and 200 mV/s, respectively. Perovskite modules were evaluated using a faster scan rate to reduce the extended testing duration. The active areas of the solar cells were defined by opaque metal masks featuring a square aperture with areas of 0.0625 cm^2 or 1.04 cm^2. For modules, the aperture areas were determined by an opaque metal mask with rectangular apertures of 27.56 cm^2.

The damp-heat stability test was performed on encapsulated devices in a sealed box with approximately 85% relative humidity (RH) and an 85°C atmosphere. Operational stability tests were conducted on glass-encapsulated solar cells under 1-sun illumination from a white LED at 85°C in the air with RH of around 50%. The epoxy from Lumen Tech. was used for the encapsulation.

The XPS instrument was calibrated using silver metal, setting the Ag 3*d*5/2 peak at 368.2 eV. A low-energy electron gun was used throughout to neutralize surface charge. In post-processing, the adventitious carbon peak at 284.8 eV was used to calibrate spectra and mitigate charging effects. Each sample was grounded using copper conductive tape, and charge compensation was performed before each measurement.

EQE spectra were acquired using an Oriel model QE-PV-SI instrument equipped with a NIST-certified Si diode. ToF-SIMS measurements were carried out on an IONTOF M6 instrument with a primary Bi source of 30 keV and an analysis area of 50 × 50 μm^2. SEM images were recorded using a JEOL JSM-7900FLV, with operating voltages of 5 kV for surface images and 15 kV for cross-section images. PL mapping was performed on a Nano Raman and TERS System integrated with SWIFT and DuoScan technologies, utilizing a 633 nm laser for excitation. CAFM was conducted on a Bruker Photocurrent and Thermal AFM with Pt/Ir-coated cantilevers, with a scan rate of 0.25 Hz and a scan area of 5 × 5 μm^2. Photoluminescence quantum yield of solid films was measured by a fiber-coupled spectrometer (QE-Pro Ocean Optics) in an integrating sphere under excitation from a power-tunable continuous wave diode laser (405 nm). The excitation light power was measured in free space using a power meter (Ophir). TRPL spectra were collected using an FS5 spectrofluorometer (Edinburgh Instruments) with an excitation wavelength of 373 nm. PXRD patterns were taken on a Rigaku Miniflex600 Diffractometer equipped with D/tex detector and a Ni-filtered Cu-Kα radiation source. Contact angle measurements were conducted on VCA Optima XE. GIWAXS measurements were performed at beamline 8ID-E at the Advanced Photon Source at Argonne National Laboratory. The samples were irradiated at incidence angles from 0.1° to 1.0° in vacuum at 10.915 keV for two summed exposures of 2.5 s each. Signals were collected with a Pilatus 1M detector located at a distance of 228.16 mm from the samples. GIWAXS data was

ACCEPTED ARTICLE PREVIEW

processed and analyzed using the GIXSGUI software for MATLAB written by Zhang Jiang and available at https://www.aps.anl.gov/Sector-8/8-ID/Operations-and-Schedules/UsefulLinks/Sector-8-GIXSGUI. CCL values were obtained using the Scherrer equation: $2\pi K/FWHM$ (where $K = 0.93$).

For the transmission electron microscopy (TEM)-based study, a cross-sectional electron-transparent lamella was prepared using a focused ion beam (FIB)-equipped scanning electron microscope (SEM-FIB Helios G5 DualBeam, FEI), with the assistance of an EasyLift nanomanipulator and a Gallium (Ga) ion source. To protect the region of interest during FIB processing, two types of protective coatings were deposited: first, a 0.5 µm layer of W coating applied using the e-beam, followed by a 3 µm layer of W coating deposited by the ion beam for final protection. The ion beam milling procedure was carried out step by step, with a beam current of 2.4 nA, 0.44 nA, 0.26 nA, 0.045 nA, and 0.025 nA, gradually reducing it from 30 kV to 5 kV, in order to cut and thin down the lamella to 60 nm while minimizing ion beam damage. Additionally, a low-current cleaning process (5-2 kV, 81-28 pA) was performed to eliminate potential contamination. Transmission Electron Microscopy (TEM)-based experiments were conducted using a Double Cs-corrected TEM Titan Themis Cubed TEM microscope operating at 80 kV. TEM data processing was carried out using Gatan™ Digital Micrograph and the Thermo Scientific™ Velox suites.

Data availability

The data supporting the findings of this study are available from the corresponding author upon request. All the crystal structure files generated in this study have been deposited at the Cambridge Crystallographic Data Center (CCDC) under the accession numbers 2362695, 2362696, 2362697, 2362698, 2362699, 2362700, 2362701, and 2362702.

Acknowledgements

This work is partially supported by award 70NANB19H005 from U.S. Department of Commerce, National Institute of Standards and Technology as part of the Center for Hierarchical Materials Design (CHiMaD). MGK was supportedby DOE BES grant DE-SC0024422 (fundamental studies on metal halides), and TJM by ONR award N00014-20-1-2116. This work made use of the SPID, EPIC, Keck-II, and NUFAB facilities of Northwestern University's NUANCE Center, which has received support from the SHyNE Resource (NSF ECCS-2025633), the Int. Institute of Nanotechnology, Northwestern University and Northwestern's MRSEC programs (NSF DMR-1720139, NSF DMR-2308691). ASRB acknowledges support from King Abdullah University of Science and Technology (KAUST) through the Ibn Rushd Postdoctoral Fellowship Award.

Author Contributions

C.L., Y.Y., and D.Z. conceived the idea and proposed the experimental design. C.L. and Y.Y. conducted the characterization. C.L., Y.Y., H.C. performed the device fabrication. I.S. performed single crystal synthesis, characterization, and structure analysis. C.L. and A.S.R.B. wrote the first draft of the manuscript. A.S.R.B. performed the SEM and XRD measurements. J.C. synthesized organic halides. I.G. conducted the PYSA measurement. B.V. and S.D.W. conducted the TEM measurement. I.G., R.P.R., T.W. and J.F. helped with the single crystal synthesis and structure

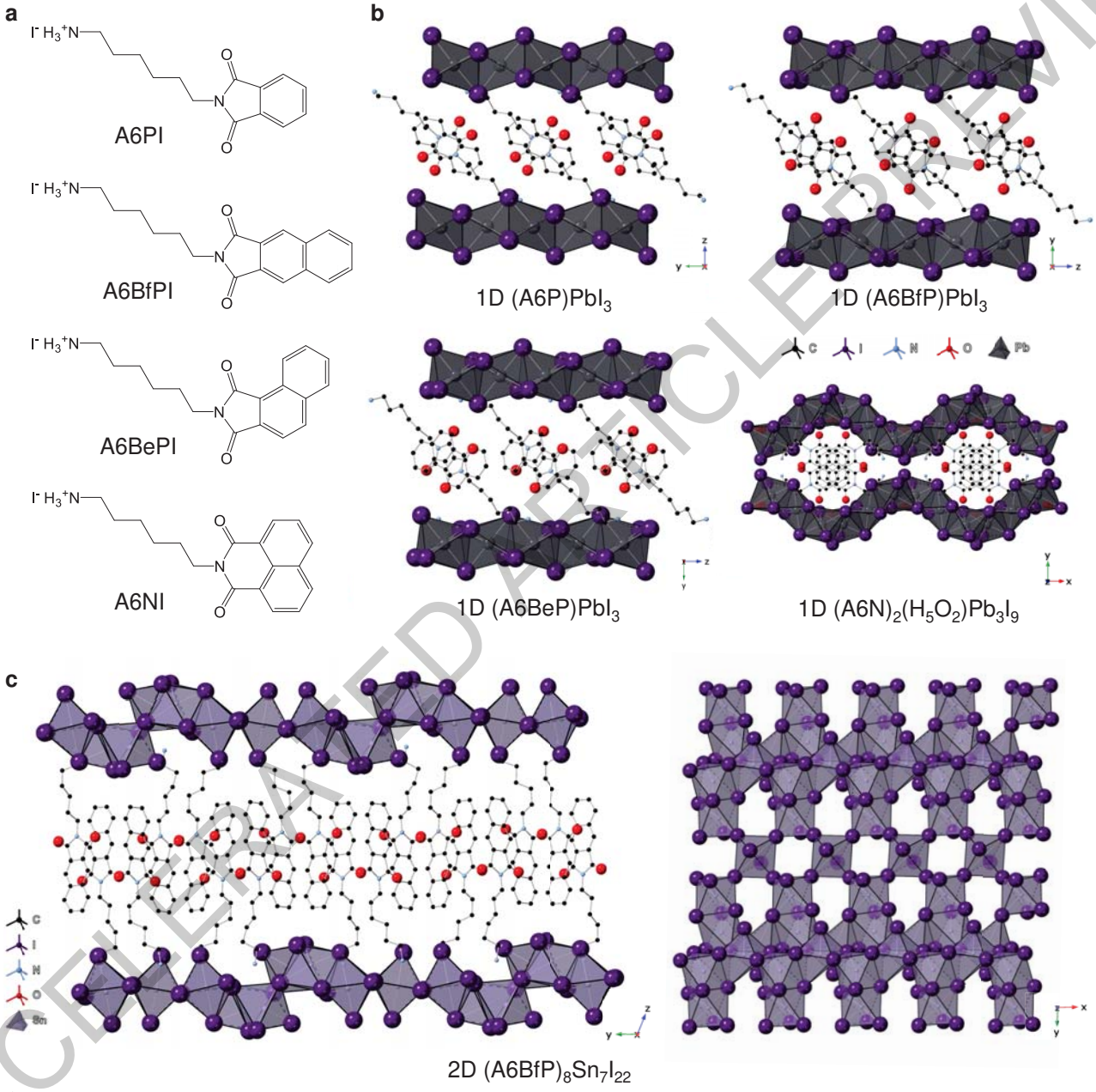
ACCELERATED ARTICLE PREVIEW

analysis. C.H. and Y.L. helped with PL measurement. A.M., Z.W., B.C., and L.X.C helped revise the manuscript. D.Z., T.J.M., A.F., E.H.S., and M.G.K. supervised the project. All the authors contributed to the revision and comments to the manuscript.

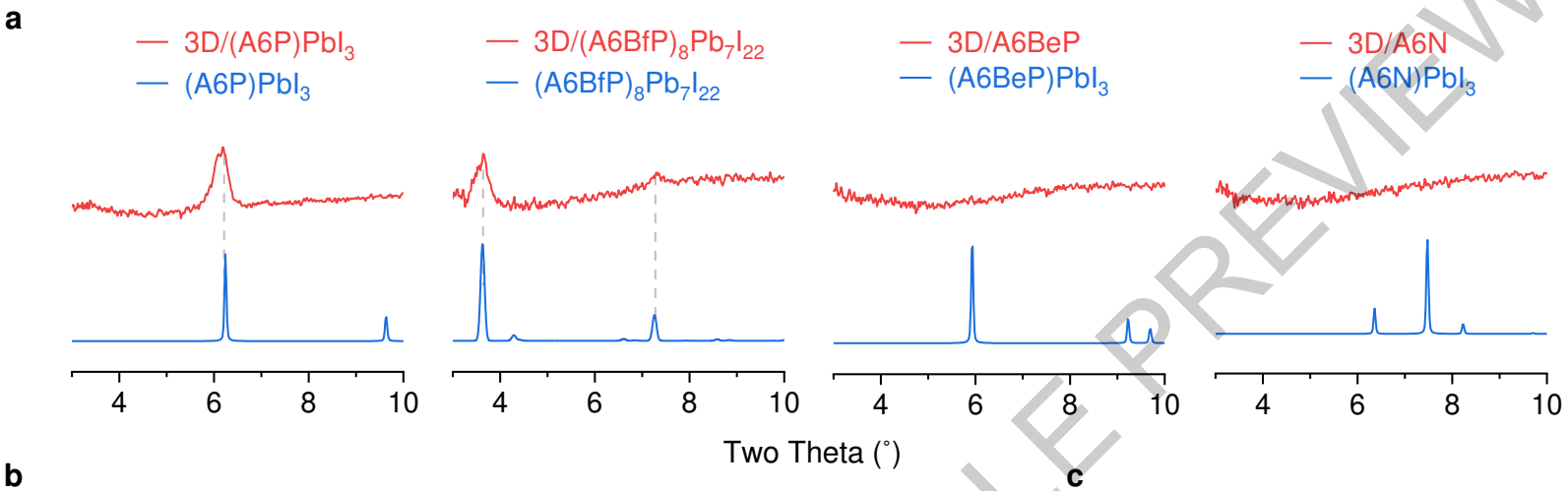
Competing Interests Statement

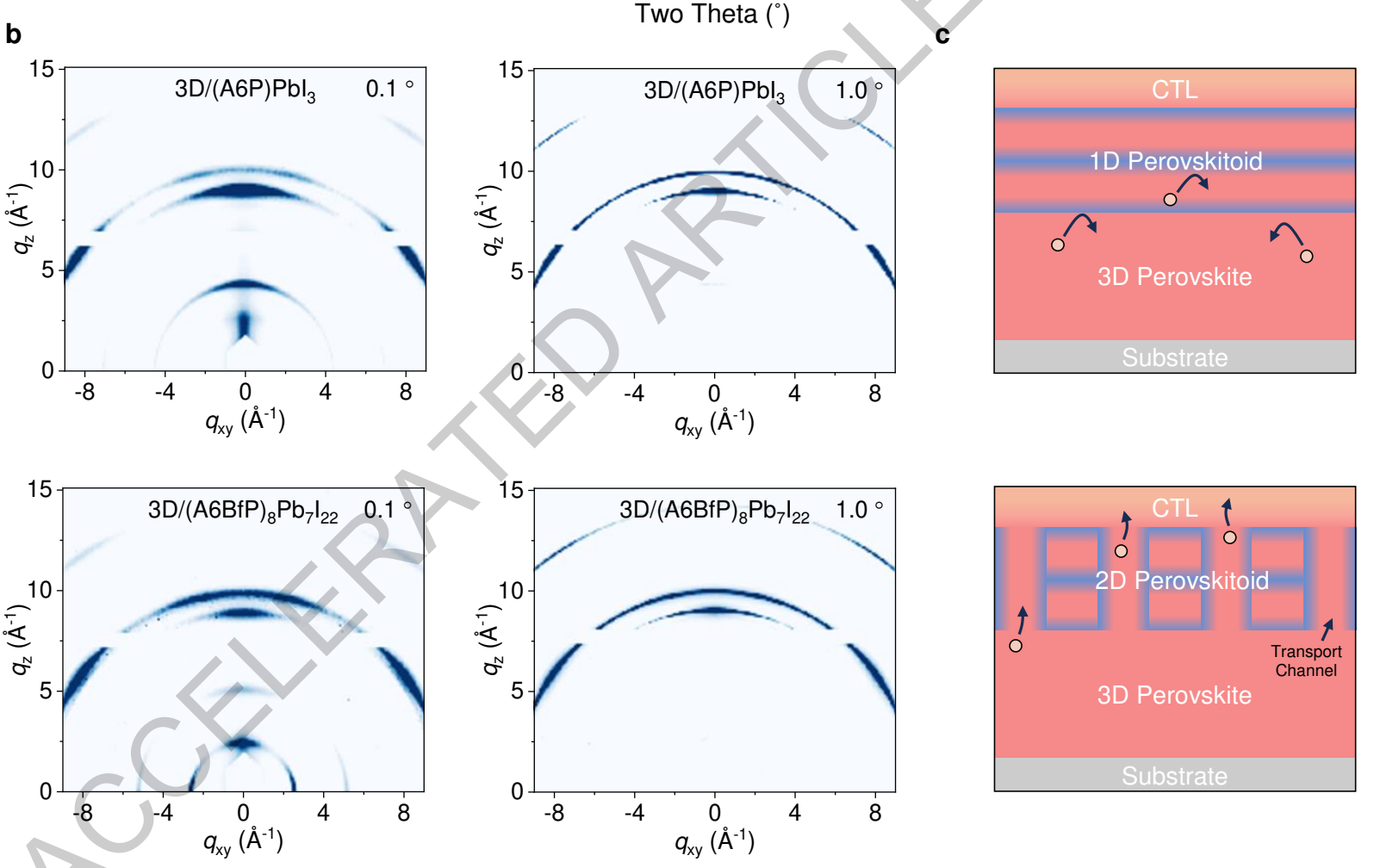
The authors declare no competing financial interests.

ACCELERATED ARTICLE PREVIEW

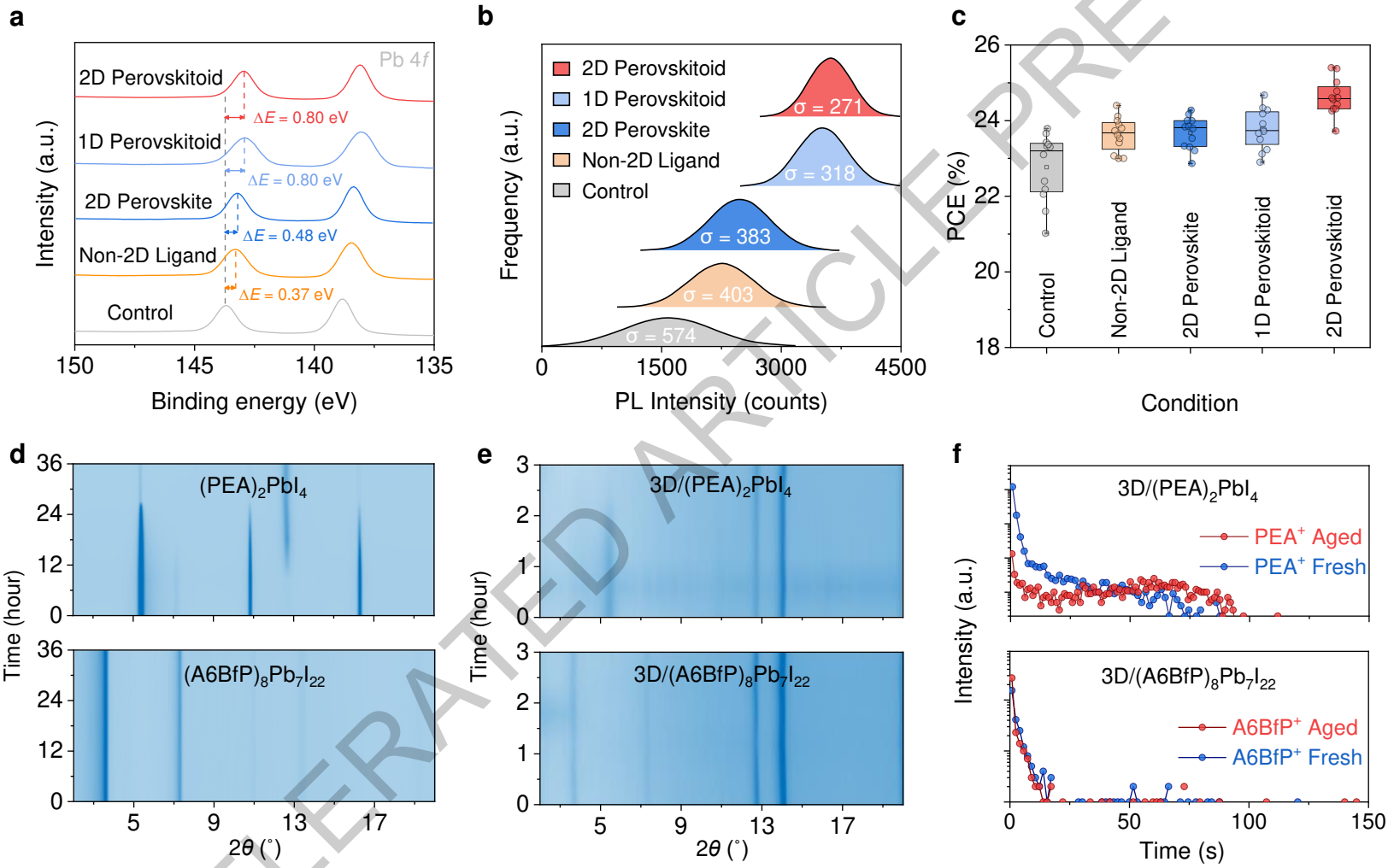


ACCELERATED ARTICLE PREVIEW

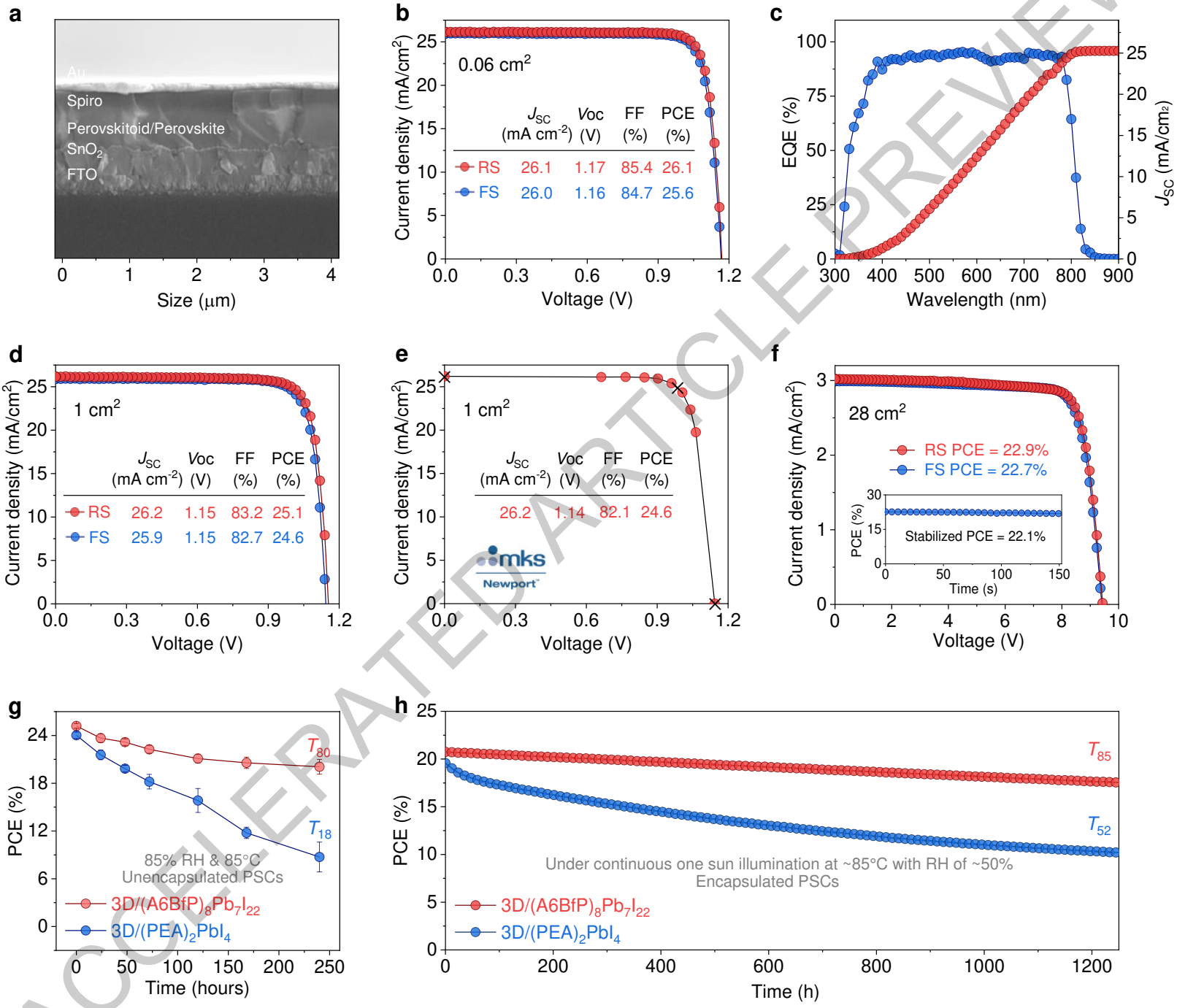




ACCELERATED ARTICLE PREVIEW



ACCELERATED ARTICLE PREVIEW



ACCELERATED ARTICLE PREVIEW

nature portfolio

Corresponding author(s): Edward H. Sargent

Solar Cells Reporting Summary

Nature Portfolio wishes to improve the reproducibility of the work that we publish. This form is intended for publication with all accepted papers reporting the characterization of photovoltaic devices and provides structure for consistency and transparency in reporting. Some list items might not apply to an individual manuscript, but all fields must be completed for clarity.

For further information on Nature Research policies, including our data availability policy, see Authors & Referees.

Experimental design

Please check the following details are reported in the manuscript, and provide a brief description or explanation where applicable.

1. Dimensions

Area of the tested solar cells	☒ Yes ☐ No	The aperture area for small-area devices, large-area devices, and large modules was 0.063, 1.04, and 27.56 cm2, respectively (Method-Characterization).
		Explain why this information is not reported/not relevant.
Method used to determine the device area	☒ Yes ☐ No	The aperture area for small-area devices, large-area devices, and large modules was 0.063, 1.04, and 27.56 cm2, respectively (Method-Characterization).
		Explain why this information is not reported/not relevant.

2. Current-voltage characterization

Current density-voltage (J-V) plots in both forward and backward direction	☒ Yes ☐ No	See Fig. 4b, d
Voltage scan conditions	☒ Yes ☐ No	The scanning step was 20 and 128 mV for solar cells and modules, respectively. The scanning rate was 70 and 200 mV/s for solar cells and modules, respectively. (Method-Characterization).
		Explain why this information is not reported/not relevant.
Test environment	☒ Yes ☐ No	Current density (J)-voltage (V) characteristics of the devices were characterized at room temperature in N2 (Method-Characterization).
		Explain why this information is not reported/not relevant.
Protocol for preconditioning of the device before its characterization	☒ Yes ☐ No	No preconditioning of the device was applied before the measurement (Method-Characterization).
		Explain why this information is not reported/not relevant.
Stability of the J-V characteristic	☒ Yes ☐ No	See Figure 4g, h
		Explain why this information is not reported/not relevant.

3. Hysteresis or any other unusual behaviour

Description of the unusual behaviour observed during the characterization	☒ Yes ☐ No	The devices showed negligible hysteresis behaviors .
		Explain why this information is not reported/not relevant.
Related experimental data	☒ Yes ☐ No	Fig.4b, d
		Explain why this information is not reported/not relevant.

4. Efficiency

External quantum efficiency (EQE) or incident photons to current efficiency (IPCE)	☒ Yes ☐ No	See Fig. 4c
		Explain why this information is not reported/not relevant.
A comparison between the integrated response under the standard reference spectrum and the response measure under the simulator	☒ Yes ☐ No	The JSC obtained from the J-V characteristics was found to be consistent with the value integrated from the external quantum efficiency (EQE) spectrum. (Fig. 4b, c).
		Explain why this information is not reported/not relevant.

For tandem solar cells, the bias illumination and bias voltage used for each subcell

☐ Yes
☒ No

Provide a description of the measurement conditions.

Explain why this information is not reported/not relevant.

5. Calibration

Light source and reference cell or sensor used for the characterization

☒ Yes
☐ No

Light source is a Xe arc lamp from a ScienceTech A1 Light Line Class AAA solar simulator. The reference solar cell is from Sciencetech (SCI-REF-Q) (Method-Characterization).

Explain why this information is not reported/not relevant.

Confirmation that the reference cell was calibrated and certified

☒ Yes
☐ No

The light intensity was calibrated by the reference solar cell (SCI-REF-Q) from Sciencetech (Method-Characterization).

Explain why this information is not reported/not relevant.

Calculation of spectral mismatch between the reference cell and the devices under test

☐ Yes
☒ No

Provide a value of the spectral mismatch and/or a description of how it has been taken into account in the measurements.

We rely on certified efficiency results.

6. Mask/aperture

Size of the mask/aperture used during testing

☒ Yes
☐ No

The active area of the solar cells was defined by opaque metal masks. The aperture area for small-area devices, large-area devices, and large modules was 0.063, 1.04, and 27.56 cm2, respectively (Method-Characterization).

Explain why this information is not reported/not relevant.

Variation of the measured short-circuit current density with the mask/aperture area

☐ Yes
☒ No

Report the difference in the short-circuit current density values measured with the mask and aperture area.

We didn't measure the solar cells with apertures of different sizes.

7. Performance certification

Identity of the independent certification laboratory that confirmed the photovoltaic performance

☒ Yes
☐ No

Newport

Explain why this information is not reported/not relevant.

A copy of any certificate(s)

☒ Yes
☐ No

Supplementary Fig. 19

Explain why this information is not reported/not relevant.

8. Statistics

Number of solar cells tested

☒ Yes
☐ No

12 devices for each condition were tested (Fig. 3c).

Explain why this information is not reported/not relevant.

Statistical analysis of the device performance

☒ Yes
☐ No

See Supplementary Fig. 15

Explain why this information is not reported/not relevant.

9. Long-term stability analysis

Type of analysis, bias conditions and environmental conditions

☒ Yes
☐ No

The damp-heat stability test was performed on encapsulated devices in a sealed box with approximately 85% relative humidity (RH) and an 85°C atmosphere. Operational stability tests were conducted on glass-encapsulated solar cells under 1-sun illumination from a white LED at 85°C in the air with RH of around 50%. The epoxy from Lumen Tech. was used for the encapsulation.

Explain why this information is not reported/not relevant.